Article:
Kanao, E., Nihei, T., Kako, K. et al. (2026) Light-activated protein-imprinted hydrogels capable of translating protein surface accessibility into missing-peptide footprints. Small Structures, 7 (6). e202600004. ISSN: 2688-4062

https://doi.org/10.1002/sstr.202600004

Small Structures

small structures

www.small-structures.com

RESEARCH ARTICLE OPEN ACCESS

Light-Activated Protein-Imprinted Hydrogels Capable of Translating Protein Surface Accessibility Into Missing-Peptide Footprints

Eisuke Kanao[1,2] | Taichi Nihei[3] | Kankichi Kako[3] | Asato Maeda[1] | Damla Ulker[4,5] | Hiroshi Nishida[1] | Kosuke Ogata[1] | Mingdi Yan[6] | Sergey Piletsky[7] | Yasushi Ishihama[1,2] | Takuya Kubo[3,8]

[1]Graduate School of Pharmaceutical Sciences, Kyoto University, Kyoto, Japan | [2]Laboratory of Proteomics for Drug Discovery, National Institute of Biomedical Innovation, Health and Nutrition, Osaka, Japan | [3]Graduate School of Engineering, Kyoto University, Kyoto, Japan | [4]School of Mathematical and Physical Sciences, University of Sheffield, Sheffield, UK | [5]Department of Pharmaceutical Basic Sciences, Near East University, Nicosia, Türkiye | [6]Department of Chemistry, University of Massachusetts Lowell, Lowell, MA, USA | [7]School of Chemistry, University of Leicester, University Road, Leicester, UK | [8]Graduate School of Life and Environmental Science, Kyoto Prefectural University, Kyoto, Japan

Correspondence: Eisuke Kanao (kanao.eisuke.7s@kyoto-u.ac.jp) | Damla Ulker (damlaulker@gmail.com) | Yasushi Ishihama (yishiham@pharm.kyoto-u.ac.jp) | Takuya Kubo (tkubo@kpu.ac.jp)

Received: 8 January 2026 | **Revised:** 24 March 2026 | **Accepted:** 13 April 2026

Keywords: hydrogel | molecular imprinting | photocrosslinking | structural proteomics

ABSTRACT

Mass spectrometry (MS)-based structural proteomics can reveal higher-order structural features in complex biological samples, but many covalent footprinting and crosslinking strategies require specialized workflows to identify modified or crosslinked species. Here, we introduce a hydrogel-based strategy that converts protein surface accessibility into a simple signal-off readout in standard label-free LC-MS/MS. We synthesize protein-permeable polyethylene glycol molecularly imprinted hydrogels (MIHs) and install perfluorophenyl azide (PFPA) photoreactive groups after polymerization. When proteins are adsorbed to the imprinted cavities, UV irradiation crosslinks nearby protein surface segments to the gel. After extensive washing and in-gel digestion, peptides from crosslinked surface regions remain trapped in the gel matrix and are therefore depleted from the recovered digest, yielding a "missing-peptide" footprint without explicit identification of crosslinked species. Lysozyme-imprinted MIHs retain template recognition and report ligand-dependent protection of a carbohydrate-binding loop. A proteome-imprinted MIH generates > 3000 protein structural fingerprints from ~ 500 ng of HEK293T lysate and detects rapamycin-dependent changes in FK506-binding proteins (FKBPs), including an FKBP4 peptide near the rapamycin-binding interface. PFPA-functionalized MIHs thus provide an aqueous solid-phase transducer that makes structural proteomics compatible with routine bottom-up workflows.

1 | Introduction

Protein three-dimensional structure and conformational dynamics underlie essentially all aspects of biological function, from enzymatic catalysis to molecular recognition and signal transduction. Classical structural biology techniques such as X-ray crystallography [1], multidimensional NMR spectroscopy [2], and cryogenic electron microscopy [3] routinely afford atomic or near-atomic models of proteins and complexes. Deep learning–based prediction methods exemplified by AlphaFold have also expanded access to structural models across the proteome [4–7]. Despite these advances, biology and drug discovery often require knowledge of how conformations and interaction surfaces are modulated by ligands, posttranslational modifications, or cellular environments in heterogeneous samples. Addressing such questions requires experimental strategies capable of probing structural features across proteomes, rather than only in purified systems.

Mass spectrometry (MS)-based proteomics can quantify thousands of proteins in complex mixtures [8, 9]. MS workflows can also report on protein structure at scale. Limited proteolysis (LiP)-MS monitors changes in protease susceptibility that depend on protein structure [10]. Thermal proteome profiling infers ligand engagement from stability shifts [11, 12]. Hydrogen-deuterium exchange (HDX)-MS provides protection and dynamics information, especially for purified systems [13]. Chemical crosslinking MS can report distance information. Covalent footprinting chemistries probe solvent accessibility and local microenvironments [14–19]. These approaches have revealed conformational changes and interaction networks, including in vivo [20, 21]. However, they involve trade-offs in sample requirements, chemistry constraints, and analysis burden. Crosslinking and labeling approaches, in particular, often require identifying modified or crosslinked peptides. Complementary approaches that remain compatible with routine bottom-up proteomics are therefore highly desirable.

Photoaffinity and photocrosslinking reagents offer a broadly applicable route to covalently capture transient contacts and solvent-exposed regions by generating highly reactive intermediates upon irradiation [22–25]. In practice, however, many photoreactive scaffolds are hydrophobic and require organic cosolvents, and the short lifetimes of photogenerated intermediates often translate into low effective crosslinking efficiencies in bulk solution [26–28]. Moreover, most proteome-scale implementations rely on identifying crosslinked species, which is analytically demanding and commonly necessitates specialized enrichment and data analysis [29, 30]. These limitations motivate strategies that increase the effective molarity of photoreactive groups at protein surfaces under aqueous conditions and that output structural information in a format directly readable by standard bottom-up proteomics.

Molecular imprinting provides a materials-based way to engineer proximity between a protein and reactive groups. In molecularly imprinted polymers (MIPs), monomers are polymerized around a template. Template removal leaves binding sites that are complementary in shape and orientation of functional groups [31–34]. Protein-targeting MIPs and protein-imprinted hydrogels operate as hydrated porous networks in aqueous media [35–39]. Polyethylene glycol (PEG)-based protein-imprinted hydrogels are biocompatible and protein-permeable. Their chemistry can be tuned with functional monomers for selective capture and sensing [40–44]. Importantly, imprinting enriches proteins within confined cavities and can preorganize functional groups near the bound surface. Postimprinting strategies further show that reporter or reactive handles can be positioned inside recognition sites [45].

Here, we developed perfluorophenyl azide (PFPA)-functionalized protein-imprinted hydrogels as solid-phase photocrosslinking reactors for converting protein surface accessibility into quantitative missing-peptide footprints (Figure 1). PFPA is a photoreactive group widely used for covalent immobilization and surface functionalization [46]. In this system, proteins captured in imprinted cavities are positioned in close proximity to PFPA-bearing polymer segments. Upon UV irradiation, exposed surface residues are covalently linked to the gel. After extensive washing and in-gel digestion, peptides derived from these crosslinked surface regions remain trapped in the hydrogel and are therefore depleted in the recovered peptide fraction, whereas peptides from noncrosslinked regions are recovered normally. By comparing MS signals from irradiated and nonirradiated gels, we obtain a missing-peptide footprint that reports higher-order structure. This footprint can be mapped onto structural models and used to detect ligand-dependent changes in surface accessibility or protein interfaces using standard label-free workflows. Compared with HDX-MS and other chemical crosslinking methods, the present method offers lower spatial precision but avoids the explicit identification of modified or crosslinked peptides and remains compatible with a routine LC-MS/MS workflow. In this respect, its output is closer to peptide-level methods such as LiP-MS, although the signal here arises from hydrogel-confined photocapture rather than altered protease susceptibility. We first demonstrate this concept using hen egg white lysozyme, and then extend it to a proteome-imprinted hydrogel prepared from HEK293T lysate, enabling proteome-wide footprinting and ligand-responsive analysis in complex samples.

2 | Results and Discussion

2.1 | Lysozyme-Based Validation of Molecular Imprinting and PFPA Functionalization of MIH

To validate that the molecularly imprinted hydrogels (MIHs) can recognize protein surface features in a sequence- and topology-dependent manner, we first employed hen egg white lysozyme as a model template. Lysozyme is a small, highly basic protein (pI ~ 11), and we therefore selected anionic functional monomers bearing sulfonate groups to promote electrostatic complementarity to the template. A series of lysozyme-imprinted hydrogels (MIH-1 to MIH-8) was prepared by varying the relative amounts of 2-acrylamido-2-methylpropanesulfonic acid (AMPS), sodium *p*-styrenesulfonate (SS), and methyl methacrylate (MMA), while keeping the PEG dimethacrylate (14G-DMA) crosslinker constant (Table 1, Structures of functional monomers are shown in Figure S6). The corresponding NIHs were synthesized in the absence of lysozyme under otherwise identical conditions.

The adsorption properties of MIHs and NIHs were evaluated using batch binding experiments in 10 mM PBS containing 50 mM NaCl. Under these conditions, MIH-5 exhibited the highest imprinting factor (adsorption capacity of a given MIH divided by that of the corresponding NIH), thus featuring the highest apparent selectivity for lysozyme (Figure S7A). As ionic strength was expected to modulate both nonspecific electrostatic interactions and the stability of the imprinted binding sites, we examined the dependence of the imprinting factor of MIH-5 on NaCl concentration, showing that the maximum was achieved at 50 mM NaCl (Figure S7B). Thus, this salt concentration provided an optimal balance between electrostatic attraction to the basic template and the suppression of charge-driven nonspecific binding. Accordingly, all subsequent lysozyme adsorption experiments were carried out in 10 mM PBS containing 50 mM NaCl.

Subsequently, the binding selectivity of MIH-5 for lysozyme was assessed in the presence of cytochrome c, trypsin, and

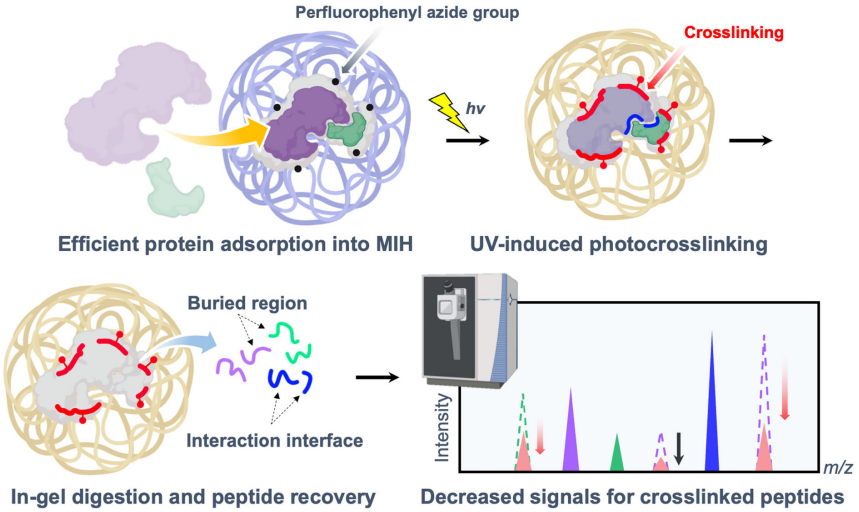

FIGURE 1 | | Concept of hydrogel-imprinting-assisted photocrosslinking for structural proteomics. Proteins are incubated in protein-imprinted PEG hydrogels that display photoreactive groups inside shape-complementary cavities. UV irradiation covalently crosslinks surface residues that contact the gel. After extensive washing and in-gel digestion, peptides not trapped in the matrix are recovered. Peptides depleted in the irradiated sample define a "missing-peptide" footprint that reports on protein higher-order structure. Part of this figure was created with BioRender.com (https://www.biorender.com/).

TABLE 1 | Compositions of the MIHs.

		Functional monomer							
	Crosslinker	AMPS, μmol	SS, μmol	MMA, μmol	MDTA, μmol	DMAEMA, μmol	Template	Initiator	Solvent
MIH-1	14G-DMA (256 μmol)	8.55	1.70	0	0	0	Lysozyme (0.57 μmol)	AIZP (2,2′-azobis[2-(2-imidazolin-2-yl)propane]) (3.09 μmol)	PBS (1.5 mL)
MIH-2		8.00	1.59	0.69	0	0			
MIH-3		7.40	1.48	1.37	0	0			
MIH-4		6.85	1.36	2.05	0	0			
MIH-5		5.70	1.14	3.42	0	0			
MIH-6		4.56	0.91	4.76	0	0			
MIH-7		2.85	0.57	6.85	0	0			
MIH-8		0	0	10.3	0	0			
MIH-9		5.7	5.7	0	3.42	0			
MIH-10	14G-DMA (128 μmol)	0	0	2.25	0.63	2.25	Cell lysate (800 μg)	AIZP (1.55 μmol)	PBS (750 μL)

peroxidase as representative nontemplate proteins with different sizes, isoelectric points, and structural features. In 50 mM NaCl, the adsorption capacity of MIH-5 for lysozyme exceeded that for the nontemplate proteins more than threefold (Figure S7C), which supports the formation of imprinted cavities that were geometrically and chemically complementary to the lysozyme surface rather than simply reflecting generic electrostatic or hydrophobic interactions.

For photocrosslinking, we introduced PFPA groups into the lysozyme-imprinted network as photoreactive handles. Upon ultraviolet (UV) irradiation, these groups generate highly reactive nitrenes that can react with C&bond;H bonds, N&bond;H bonds, and aromatic rings on nearby proteins; however, PFPA-containing monomers are typically overly hydrophobic for the direct aqueous free-radical polymerization of PEG-based hydrogels [46]. To circumvent this limitation, we used a water-soluble disulfide-containing methacrylamide monomer, ({[2-(2-methacrylamido)ethyldithio]ethylcarbamoyl}methoxy)acetic acid (MDTA), as a latent thiol-bearing functional monomer. MIH-9 was prepared by replacing MMA with MDTA in the lysozyme MIP formulation (Table 1) and thus contained disulfide linkages that could later be reduced to free thiols (Figure 2A). Despite this substitution, MIH-9 retained template-selective binding. Specifically, MIH-9 adsorbed more lysozyme than the corresponding nonimprinted hydrogel (NIH) (Figure 2B) and preferentially bound lysozyme over nontemplate proteins under identical conditions (Figure 2C).

Subsequently, PFPA groups were introduced into MIH-9 via a postpolymerization reaction. The reduction of the MDTA disulfide bonds with tris(2-carboxyethyl)phosphine (TCEP) generated

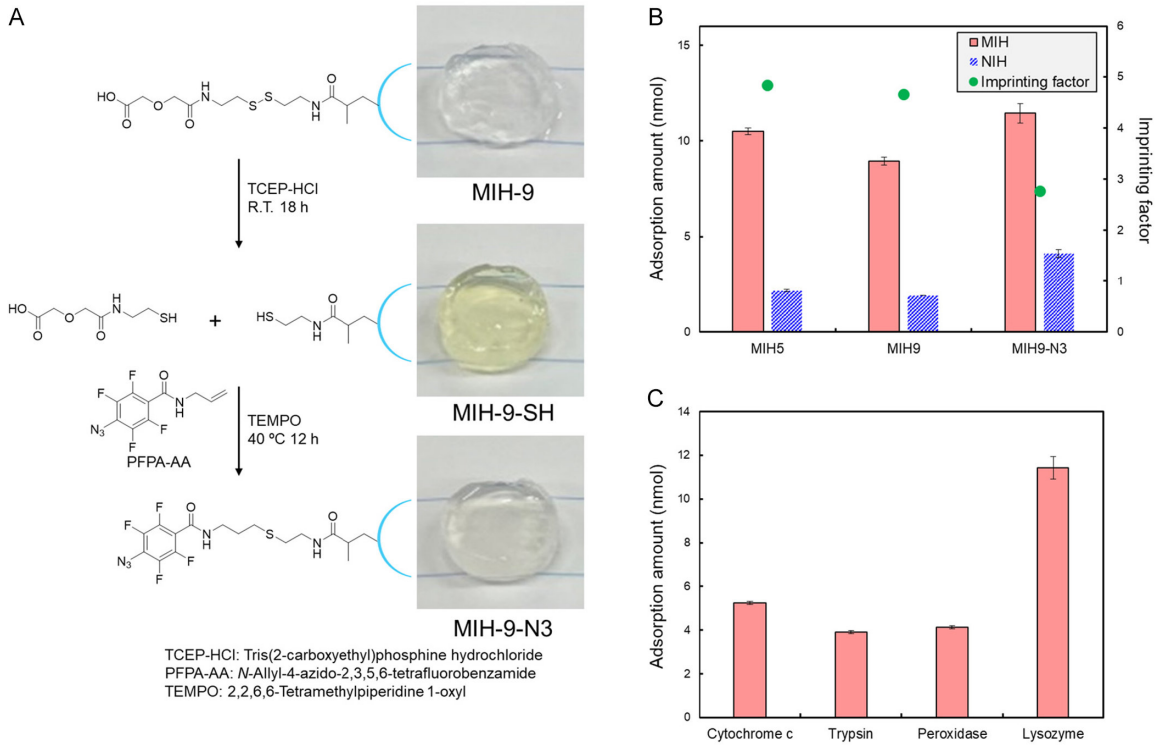

FIGURE 2 | | Introduction of perfluorophenyl azide (PFPA) groups into lysozyme-imprinted hydrogels and preservation of molecular recognition. (A) Schematic of the postpolymerization functionalization strategy applied to lysozyme-imprinted hydrogels. (B) Protein adsorption capacities of MIH-5, MIH-9, PFPA-functionalized MIH-9 (MIH-9-N3), and the corresponding nonimprinted hydrogels. (C) Adsorption capacities of MIH-9-N3 for lysozyme and control proteins. Data are presented as means ± standard deviations (SDs; $n = 3$ gel discs per condition).

thiol groups within the hydrogel network, which were then reacted with a PFPA-containing monomer to afford a PFPA-functionalized hydrogel (MIH-9-N3, Figure 2A). Reaction progress was accompanied by a gel color change, and MIH-9-N3 retained the preference of MIH-9 precursor for lysozyme adsorption (Figure 2B,C), which indicated that the introduction of PFPA groups did not compromise the imprinted binding sites. Notably, the imprinting factor decreased after PFPA coupling (Figure 2B). This decrease is likely attributable to increased nonspecific adsorption arising from the hydrophobic perfluoroaryl PFPA moieties, which increase background binding on the nonimprinted hydrogel and thereby lower the MIH/NIH ratio. Importantly, MIH-9-N3 still showed higher lysozyme adsorption than the corresponding NIH and retained preferential binding to the template protein, indicating that the imprinted recognition remains functional after PFPA functionalization.

To confirm the introduction of PFPA and consumption of thiol functionalities, we employed Ellman's reagent and infrared spectroscopy. The thiol contents of MDTA-containing MIHs before and after PFPA coupling were evaluated by immersing them in Ellman's reagent solution and recording their absorbance at 412 nm according to the manufacturer's protocol (Figures S8A and B) to assess reaction progress. A new band around 2100 cm^{-1} emerged in the attenuated total reflection infrared spectroscopy spectra of the hydrogels after PFPA functionalization (Figure S8C), consistent with the azide stretching vibration of the perfluorophenyl azide group. Collectively, these results demonstrate that azide-bearing lysozyme-imprinted hydrogels constructed via MDTA-mediated postpolymerization functionalization retained the ability to recognize the template protein, thereby providing a suitable platform for subsequent photocrosslinking-based structural proteomics.

2.2 | Structural Analysis of Lysozyme in MIH-9-N3

We next examined the ability of MIH-9-N3 to convert higher-order structural information into peptide-level MS readouts. Lysozyme-loaded MIH-9-N3 discs were irradiated at 365 nm, and the protein released after high-salt washing was quantified. Prior to UV irradiation, >98% of the lysozyme adsorbed by MIH-9-N3 (8.4 nmol) was recovered by elution with 1.0 M NaCl, which indicates a largely reversible adsorption. After UV exposure, the amount of recovered lysozyme decreased to <3% of the adsorbed amount (~0.24 nmol), indicating efficient covalent immobilization of lysozyme within the PFPA-modified hydrogel network (Figure 3A).

To examine the effects of this photocrosslinking on the peptide spectrum, we compared peptide abundances obtained for lysozyme-loaded MIH-9-N3 with and without UV irradiation. After in-gel proteolysis, equal peptide amounts (150 ng) were analyzed by LC-MS/MS. Among the quantified lysozyme-derived peptides, two peptides (HGLDNYR and WWCNDGR) were significantly depleted upon UV irradiation, whereas two peptides (GYSLGNWVCAAK and NTDGSTDYGIQINSR) increased relative to the nonirradiated control (Figure 3B). Thus, MIH-assisted photocrosslinking did not uniformly weaken the signals of all surface peptides but produced a characteristic pattern, with the recovered digest depleted in some peptides and enriched in others.

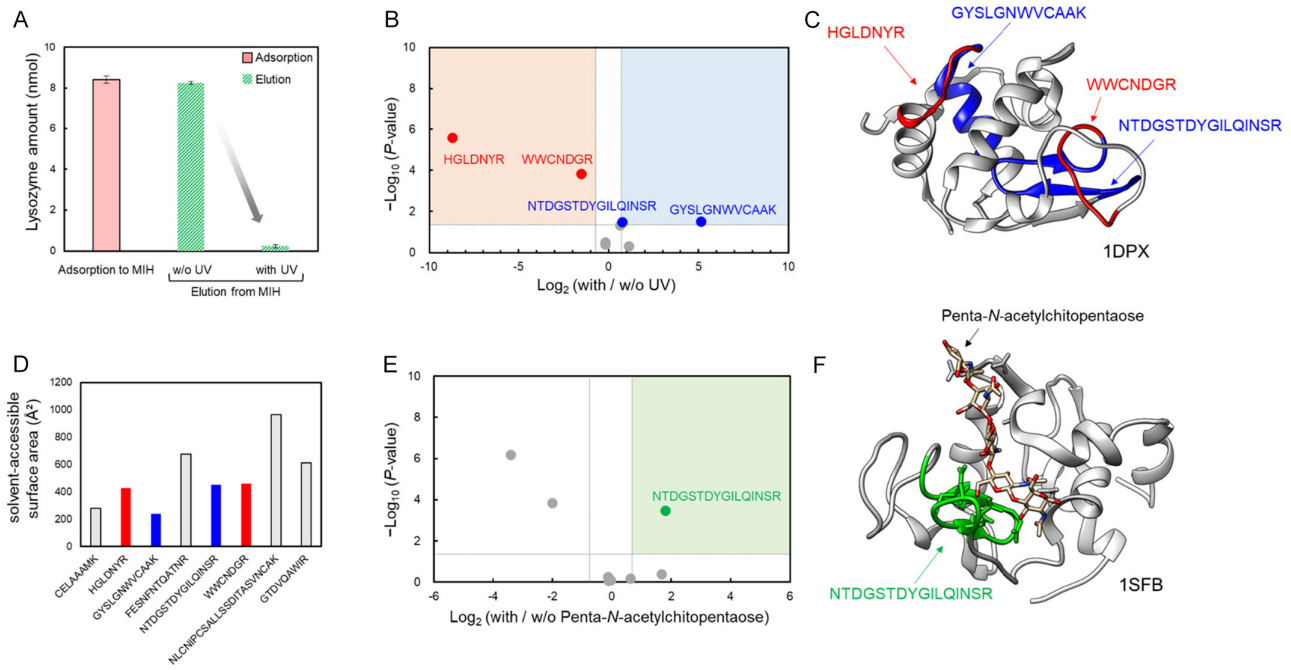

FIGURE 3 | | Structural analysis of lysozyme using PFPA-functionalized MIHs. (A) Quantification of lysozyme adsorbed to and eluted from MIH-9-N3. Bars represent means ± SDs ($n = 3$ discs). (B) Volcano plot of lysozyme-derived peptides comparing crosslinked and noncrosslinked MIH-9-N3. Dashed lines indicate cutoff values of $|\log_2(\text{fold change})| = 0.75$ and $P = 0.05$. (C) Structural mapping of UV-responsive peptides on lysozyme (PDB 1DPX). Peptides downregulated and upregulated upon UV irradiation are highlighted in red and blue, respectively. (D) SASAs of lysozyme-derived peptides. (E) Volcano plot of peptide abundances for lysozyme crosslinked in the presence or absence of penta-*N*-acetylchitopentaose. (F) Mapping of the ligand-responsive peptide onto the lysozyme–penta-*N*-acetylchitopentaose complex (PDB 1SFB).

Because equal peptide amounts were injected for LC-MS/MS, this comparison is intrinsically compositional. Depletion of strongly trapped peptides can make unaffected or less affected peptides appear relatively increased. In addition, photocrosslinking may locally alter protease access and peptide release, thereby redistributing signal across neighboring sequence segments.

The mapping of these four peptides onto the lysozyme structure (PDB 1DPX) showed that they occupy different regions of the protein surface (Figure 3C). The structure was visualized using Chimera v. 1.19 [47]. The downregulated peptides (HGLDNYR and WWCNDGR) form contiguous segments on one face of the molecule in proximity to helices and loops expected to engage the hydrogel matrix. By contrast, the upregulated peptides (GYSLGNWVCAAK and NTDGSTDYGIQINSR) trace a separate region spanning an α-helix and β-strand/loop near the central cleft. The per-peptide solvent-accessible surface areas (SASAs) calculated based on the 1DPX structure reveal that (i) the UV-sensitive peptides are generally more exposed than peptides whose intensities changed little and (ii) the average SASAs of the upregulated peptides minimally exceed those of the downregulated ones (Figure 3D). Although only a limited number of peptides achieved statistical significance at the current sequencing depth, these data indicate that PFPA-mediated crosslinking within MIHs is sensitive to the local structural environment of lysozyme and that the resulting peptide-level changes can be interpreted in terms of three-dimensional surface topology.

To examine the ability of our approach to detect perturbations at a defined interaction site, we repeated the experiment in the presence of penta-*N*-acetylchitopentaose, a well-characterized chitooligosaccharide ligand of lysozyme [48]. MIH-9-N3 discs were equilibrated with lysozyme and penta-*N*-acetylchitopentaose at a fivefold molar excess (to promote near-saturation binding under diffusion-limited gel conditions) before UV irradiation and digestion, and peptide intensities obtained for ligand-bound and ligand-free crosslinked samples were compared. A single peptide, NTDGSTDYGIQINSR, was notably upregulated in the presence of penta-*N*-acetylchitopentaose (Figure 3E). Structural mapping onto the lysozyme–chitopentaose complex (PDB 1SFB) showed that this peptide corresponds to a loop segment lining the canonical carbohydrate-binding cleft and includes residues directly contacting chitooligosaccharides (Figure 3F). Thus, the occupation of this cleft by penta-*N*-acetylchitopentaose was concluded to sterically shield or reorient the surface relative to the PFPA groups in the hydrogel, thereby reducing the extent of photocrosslinking at this segment and increasing the recovery of the corresponding peptide. Collectively, the lysozyme and ligand-binding data confirm the ability of PFPA-functionalized MIHs to encode both protein surface topology and specific protein–ligand interactions into quantitative peptide-level MS signals under aqueous conditions.

2.3 | Proteome-Wide Application of MIH-Assisted Photocrosslinking

Encouraged by the lysozyme results, we explored whether PFPA-functionalized MIHs can be used for the proteome-wide structural footprinting of cell lysates. A proteome-imprinted hydrogel (MIH-10) was prepared by polymerizing the PEG-based network in the presence of HEK293T cell lysate as the template. In contrast to the lysozyme MIHs, MIH-10 was designed to accommodate a

broad range of protein surface chemistries; therefore, the cationic monomer DMAEMA was included in addition to AMPS, SS, MMA, and MDTA. PFPA groups were introduced into MIH-10 via the MDTA/TCEP-mediated strategy described above to afford MIH-10-N3. Although the MIH/NIH ratio was smaller than in the single-protein (lysozyme) system, MIH-10-N3 consistently adsorbed more total HEK293T lysate protein than the nonimprinted control, providing sufficient enrichment for photocrosslinking and LC-MS/MS readout (Figure 4A). When lysate-loaded MIH-10-N3 was irradiated at 365 nm and then washed with 1.0 M NaCl, the recovery of adsorbed proteins was 22% (cf. 97% for the nonirradiated control) (Figure 4A), which demonstrated the efficient photocrosslinking of a substantial proteome fraction to the hydrogel matrix. Peptides released from crosslinked and noncrosslinked MIHs were analyzed by LC-MS/MS using matched peptide injection amounts (150 ng). Considering only proteins identified in at least two of the three biological replicates, we identified 3274 proteins for the nonirradiated condition and 3242 for the irradiated condition, with 3178 quantified for both conditions (Figure S9). Thus, MIH-10-N3 enabled proteome-scale structural readouts from minimal input material [as little as 500 ng of lysate (~2000 cells) per MIH adsorption assay].

To assess the effects of photocrosslinking on peptide-level signals, we focused on peptides quantified in both irradiated and nonirradiated samples among the 3178 shared proteins (Figure S9). The corresponding volcano plot revealed that the levels of 4684 peptides (originating from 2115 proteins) markedly decreased upon UV irradiation, whereas those of 179 peptides (175 proteins) notably increased (Figure 4B). This asymmetric distribution indicates that PFPA-mediated crosslinking within MIH-10-N3 predominantly weakened the peptide signal. In this respect, our readout is signal-off: Unlike previous MIP-based surface/epitope mapping approaches, which identify a recovered subset of protected fragments (signal-on) [49–53], PFPA-MIH footprinting encodes accessibility mainly as selective peptide signal weakening within an otherwise standard label-free proteomics workflow.

The strong asymmetry between the downregulated and upregulated peptides is also mechanistically informative. Because equal peptide amounts were analyzed, depletion of strongly trapped peptides can generate relative increases in other peptides through compositional rebalancing. Additional increases may arise from local redistribution of proteolysis and peptide release around immobilized regions or from indirect structural effects of photocrosslinking. We therefore regard the upregulated peptides in this comparison as secondary features, whereas the downregulated peptides constitute the primary structural readout of the method. In addition, because MIH-10-N3 was designed as a broadly permissive capture matrix rather than a cavity set enforcing a unique binding pose for any one protein, the resulting peptide depletion

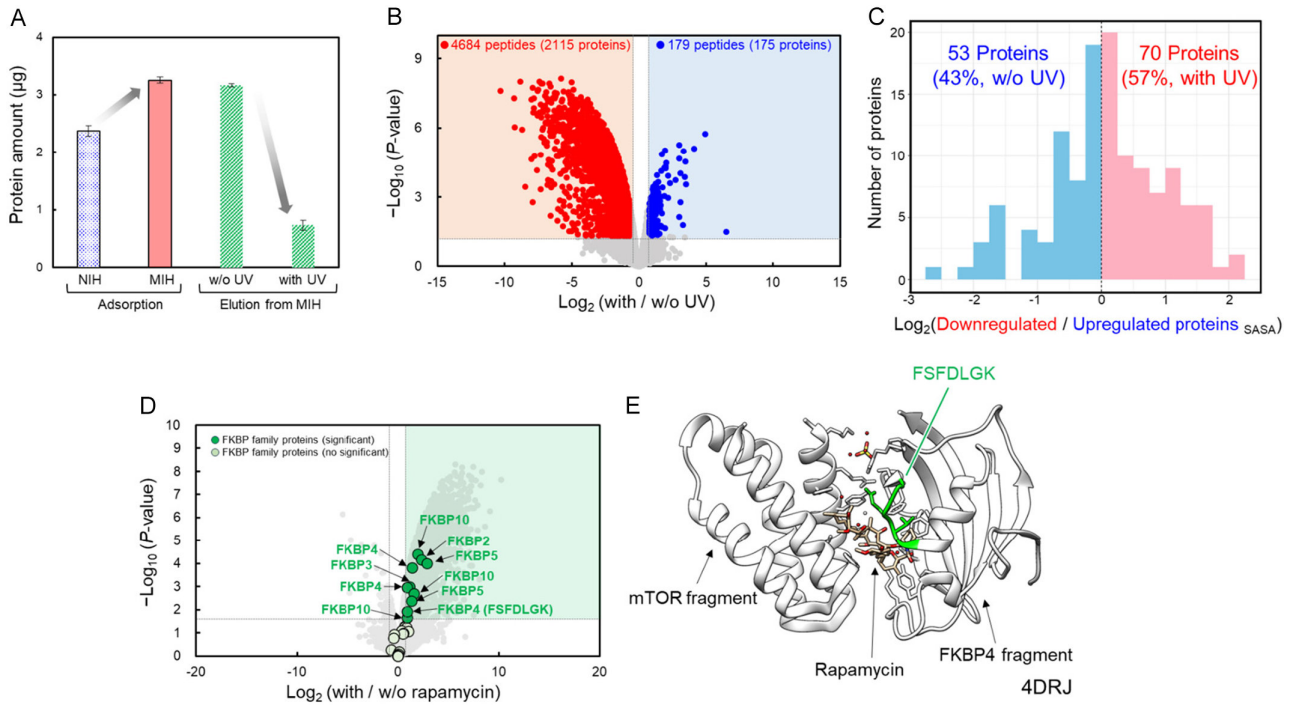

FIGURE 4 | | Proteome-wide structural footprinting and rapamycin-dependent interactions in HEK293T lysates revealed using PFPA-functionalized MIH-10 (MIH-10-N3). (A) Adsorption and photocrosslinking behavior of HEK293T cell lysate proteins on MIH-10-N3. Bars show the amounts of protein adsorbed by MIH-10-N3 and the corresponding nonimprinted hydrogel (left), as well as the amount of protein eluted from MIH-10-N3 without or with UV irradiation at 365 nm (right). (B) Volcano plot of peptide abundances for proteins shared between UV-irradiated and nonirradiated MIH-10-N3 samples. Red points denote 4684 UV-downregulated peptides (2115 proteins), and blue points denote 179 UV-upregulated peptides (175 proteins). (C) Distribution of SASA differences between UV-downregulated and UV-upregulated peptides within the same proteins. (D) Rapamycin-dependent peptide responses in HEK293T lysates. Volcano plot comparing peptide intensities between UV-crosslinked MIH-10-N3 samples treated with 5 μM rapamycin versus vehicle control. Significantly affected peptides from FKBP family proteins ($\log_2$ (fold change) ≥ 0.75, $P < 0.05$) are highlighted in green, and other FKBP family proteins are colored light green. (E) Structural mapping of a rapamycin-responsive peptide from FKBP4.

should be interpreted as reflecting the combined effects of protein capture, local PFPA proximity, surface exposure, and productive photocrosslinking and recovery, rather than surface accessibility alone. Thus, the proteome-scale output is best viewed as an ensemble-averaged, accessibility-biased peptide footprint rather than a residue-level contact map. In practical terms, confidence is highest when multiple depleted peptides from the same protein converge on one surface region, whereas isolated peptide events are best treated as hypothesis-generating.

We next examined whether UV-downregulated peptides correspond to more solvent-exposed segments than UV-upregulated ones. For the 123 proteins that contained at least one significantly downregulated and one significantly upregulated peptide, we computed the SASA of each peptide using FreeSASA [54] and monomeric structural models from the AlphaFold Protein Structure Database [5, 55]. When multiple peptides of the same class were present for a given protein, peptide-level SASAs were averaged within each class. Across these 123 proteins, 70 (57%) showed larger mean SASAs for UV-downregulated peptides than for UV-upregulated ones, whereas 53 (43%) showed the opposite trend (Figure 4C). Although this effect was modest, the bias toward greater solvent exposure among UV-downregulated peptides supports the notion that MIH-assisted photocrosslinking preferentially reports on surface-accessible regions at the proteome level. The limited effect size likely reflects gel heterogeneity, orientation averaging, nonuniform PFPA reactivity, peptide-specific biases in recovery and detectability, and the use of static structural models. Moreover, because proteins were analyzed after cell lysis rather than in a fully native cellular environment, the measured accessibility does not necessarily coincide with endogenous surface presentation for all protein classes, particularly those whose conformations depend on membranes or higher-order assemblies. Accordingly, our strategy should be interpreted as providing a statistical enrichment for accessible regions rather than a deterministic readout of direct contact.

Finally, we examined whether proteome-imprinted MIH-10-N3 could detect ligand-dependent structural changes and protein–ligand interactions. As a test case, we used rapamycin, which forms ternary complexes with FKBP12 and the FKBP12-rapamycin-binding (FRB) domain of mTOR and, more broadly, can recruit several larger FKBP family members into analogous complexes with mTOR [56]. MIH-10-N3 was incubated with HEK293T lysates in the presence or absence of 5 μM rapamycin and then subjected to UV irradiation, in-gel digestion, and LC-MS/MS analysis. Rapamycin treatment had little effect on global coverage: 3090 proteins and 11 172 peptides were consistently identified across all three datasets (Figure S9).

Despite this overall similarity, the rapamycin condition produced a distinct subset of peptides with significantly altered abundances. A volcano plot comparing UV-crosslinked samples with and without rapamycin treatment highlighted a cluster of peptides derived exclusively from FKBP family proteins (FKBP1A, FKBP1B, FKBP3, FKBP4, FKBP5, and FKBP10), all of which were significantly upregulated in the presence of rapamycin (Figure 4D). Notably, mTOR itself was not confidently identified under our conditions, which implies that the observed effects arise from local changes in FKBP surfaces rather than from the altered capture of mTOR.

Among the FKBP-derived peptides, FSFDLGK from FKBP4 was one of the rapamycin-upregulated species. The mapping of this peptide onto the crystal structure of the FKBP4-rapamycin–FRB complex (PDB 4DRJ) [57] revealed that it is adjacent to the rapamycin- and FRB-binding interface on the PPIase domain (Figure 4E). This positioning suggests that rapamycin binding and ternary complex formation shield or reorganize this surface relative to PFPA groups in the hydrogel, thereby reducing the extent of photocrosslinking and increasing the recovery of FSFDLGK in the digest, in analogy to the behavior observed for the lysozyme–chitopentaose interaction. Collectively, these data indicate that PFPA-functionalized proteome-imprinted hydrogels can capture proteome-wide surface accessibility patterns and report on ligand-induced changes in protein interfaces in complex lysates.

3 | Conclusion

PFPA-functionalized protein-imprinted PEG hydrogels provide a novel research platform that converts protein surface accessibility into a simple, MS-readable "missing-peptide" footprint. Using MDTA as a latent thiol handle, we introduced PFPA groups postpolymerization while preserving template-selective binding. In the lysozyme model, MIH-assisted photocrosslinking generated reproducible peptide-level footprints that mapped to surface topology and reported ligand-dependent protection at the carbohydrate-binding cleft. Extending the concept to a proteome-imprinted hydrogel, we obtained >3000 protein structural fingerprints from ~500 ng of HEK293T lysate and detected rapamycin-responsive peptides across endogenous FKBP family proteins, including an FKBP4 segment adjacent to the rapamycin–FRB interface. Unlike conventional crosslinking or footprinting workflows, our approach does not require enrichment or explicit identification of crosslinked peptides and is compatible with routine label-free bottom-up proteomics. We anticipate that PFPA-functionalized MIHs will complement existing structural proteomics methods by enabling rapid, aqueous, and scalable screening of ligand binding and interface changes directly in complex samples.

4 | Experimental Section

4.1 | Materials

PEG 600 dimethacrylate (14G-DMA), functional monomers, and other reagents were used as received unless noted. MDTA was prepared as reported previously (Figure S1) [45]. The synthesis and characterization of *N*-allyl-4-azido-2,3,5,6-tetrafluorobenzamide (PFPA-AA) are described in the Supporting Information (Figures S1–S5). HEK293T cells were cultured under standard conditions. Cell pellets were lysed in ice-cold 10 mM phosphate-based buffer (pH 7.3) supplemented with protease/phosphatase inhibitors and an RNase inhibitor, homogenized by needle passage, and clarified by centrifugation (20000 g, 20 min, 4°C). Protein concentrations were determined using the Pierce BCA Protein Assay.

4.2 | Hydrogel Preparation and Postpolymerization Introduction of PFPA Groups

PEG-based hydrogels were prepared by the photopolymerization (365 nm, 3 h) of 14G-DMA with functional monomers and AIZP in 10 mM PBS with or without template protein/lysate (Table 1). Gel rods were sliced into ~1 mm–diameter discs, washed with 1.0 M NaCl (24 h × 3) to remove templates, and equilibrated in 10 mM PBS. MDTA-containing hydrogels were reduced with TCEP (50 mM, 10 mM phosphate buffer with pH 6.3, 12 h), thoroughly rinsed, functionalized with PFPA-AA in H_2O/DMSO (1:1) in the presence of TEMPO (40°C, 24 h) under N_2, and extensively washed with 10 mM PBS.

4.3 | Protein Adsorption and Photocrosslinking

For adsorption assays, gel discs were equilibrated in 10 mM PBS containing 50 mM NaCl and incubated with protein solutions (typically 200 μg/mL, 1 mL, 24 h). For footprinting experiments, gel blocks (5 × 5 × 1 mm) were incubated with protein solutions (typically 5 μg/mL, 100 μL, 24 h). Photocrosslinking was performed by UV irradiation at 365 nm for 5 min (lamp positioned ~ 5 cm from the solution surface) followed by thorough washing with 10 mM PBS containing 1.0 M NaCl to remove noncovalently bound proteins.

4.4 | In-Gel Digestion

Samples were processed using the ConGnaC-Tip workflow [58] combined with a phase-transfer surfactant (PTS)-aided digestion protocol [59]. Briefly, gels and solutions were suspended in PTS buffer, reduced (DTT) and alkylated (IAA), digested with Lys-C followed by trypsin, and subjected to phase transfer with ethyl acetate/TFA. Residual peptides were extracted from gels with acetonitrile/NaCl/TFA. Combined peptide fractions were dried and desalted using StageTips [60, 61] before LC-MS/MS analysis. Peptide concentrations were also measured using a NanoDrop instrument (Thermo Fisher Scientific) based on absorption at 205 nm, assuming an extinction coefficient of 31 [62]. For LC-MS/MS analysis, 150 ng of peptides was injected per analysis.

4.5 | Nano-LC-MS/MS and Data Processing

Peptides were analyzed using an Ultimate 3000 system coupled to an Orbitrap Exploris 480 mass spectrometer with FAIMS Pro. Separation was achieved on a self-packed C18 column [63] using a 5–40% solvent B gradient over 30 min (solvent A: 0.5% acetic acid; solvent B: 0.5% acetic acid in 80% acetonitrile), with signals acquired at FAIMS CV −40/−60 under data-dependent conditions. Raw files were processed using MaxQuant [64] (v1.6.17.0) with the Andromeda search engine [65] against the human UniProt database (release 2025_12) supplemented with the lysozyme sequence and common contaminants. Raw data files acquired in FAIMS experiments were initially converted into MaxQuant-compatible mzXML files using the FAIMS MzXML Generator (https://github.com/coongroup/FAIMS-MzXML-Generator) [66]. The false discovery rate was controlled at 1% at peptide spectrum match and protein levels. Label-free quantification used "unique plus razor" peptides; match-between-runs was enabled with default settings. For volcano plots, peptide levels were considered significantly changed at $p \leq 0.05$ and $|\log_2(\textit{fold change})| > 0.75$. Additional parameters and details are given in the Supporting Information.

Author Contributions

Takuya Kubo: conceptualization (lead); funding acquisition (lead); investigation (lead); methodology (equal); supervision (lead); writing – original draft (equal); writing – review & editing (lead). **Eisuke Kanao**: conceptualization (lead); data curation (lead); formal analysis (lead); funding acquisition (equal); writing – original draft (lead); writing – review & editing (equal). **Taichi Nihei**: data curation (lead). **Kankichi Kako**: data curation (lead). **Asato Maeda**: data curation (equal). **Damla Ulker**: conceptualization (supporting); validation (supporting). **Hiroshi Nishida**: data curation (equal); methodology (equal). **Kosuke Ogata**: conceptualization (equal); formal analysis (equal). **Mingdi Yan**: conceptualization (supporting); methodology (supporting). **Sergey Piletsky**: conceptualization (supporting); formal analysis (supporting); supervision (supporting). **Sergey Piletsky**: conceptualization (supporting); formal analysis (supporting); supervision (supporting). **Yasushi Ishihama**: funding acquisition (supporting); supervision (equal); writing review & editing (equal).

Acknowledgments

The authors acknowledge support from the AMED-PRIME program (JP24gm7010003 to E.K.), AMED Interstellar Initiative (25jm0610109h0001 to E.K.), NEDO Intensive Support Program for Young Promising Researchers (seeds-4891 to E.K.), Grants-in-Aid for Scientific Research (KAKENHI; JP26K02156, 23H04924, 25K22526 JP23K13774, JP21K14652, and JP20K20567 to E.K.; JP20K21478 to Y.I.), Incubation Program Advance of Kyoto University (to E.K. and T.K.), Toyota Riken Scholar (to E.K.), Takeda Science Foundation (to E.K.), JST-ASTEP (JPMJTR25U9 to E.K. and JPMJTR214C to T.K.), JST-CREST (JPMJCR2332 to T.K.), and JST SPRING (JPMJSP2110 to A.M.).

Conflicts of Interest

The authors declare no conflicts of interest.

Data Availability Statement

The data that support the findings of this study are available on request from the corresponding author. The data are not publicly available due to privacy or ethical restrictions. The LC-MS/MS data have been deposited to the ProteomeXchange Consortium via the jPOST partner repository (https://jpostdb.org) [67] with the data set identifier PXD071903.

References

1. G. Brändén and R. Neutze, "Advances and Challenges in Time-Resolved Macromolecular Crystallography," *Science* 373 (2021): eaba 0954.

2. Y. Hu, K. Cheng, L. He, et al., "NMR-Based Methods for Protein Analysis," *Analytical Chemistry* 93 (2021): 1866.

3. H. R. Saibil, "Cryo-EM in Molecular and Cellular Biology," *Molecular Cell* 82 (2022): 274.

4. A. W. Senior, R. Evans, J. Jumper, et al., "Improved Protein Structure Prediction Using Potentials from Deep Learning," *Nature* 577 (2020): 706.

5. J. Jumper, R. Evans, A. Pritzel, et al., "Highly Accurate Protein Structure Prediction with AlphaFold," *Nature* 596 (2021): 583.

6. K. Tunyasuvunakool, J. Adler, Z. Wu, et al., "Highly Accurate Protein Structure Prediction for the Human Proteome," *Nature* 596 (2021): 590.

7. M. Baek, F. DiMaio, I. Anishchenko, et al., "Accurate Prediction of Protein Structures and Interactions Using a Three-Track Neural Network," *Science* 373 (2021): 871.

8. R. Aebersold and M. Mann, "Mass Spectrometry-Based Proteomics," *Nature* 422 (2003): 198.

9. A. Pandey and M. Mann, "Proteomics to Study Genes and Genomes," *Nature* 405 (2000): 837.

10. S. Schopper, A. Kahraman, P. Leuenberger, et al., "Measuring Protein Structural Changes on a Proteome-Wide Scale Using Limited Proteolysis-Coupled Mass Spectrometry," *Nature Protocols* 12 (2017): 2391.

11. M. M. Savitski, F. B. M. Reinhard, H. Franken, et al., "Tracking Cancer Drugs in Living Cells by Thermal Profiling of the Proteome," *Science* 346 (2014): 1255784.

12. A. Mateus, J. Bobonis, N. Kurzawa, et al., "Thermal Proteome Profiling in Bacteria: Probing Protein State *in vivo*," *Molecular Systems Biology* 14 (2018): e8242.

13. L. Konermann, J. Pan, and Y.-H. Liu, "Hydrogen Exchange Mass Spectrometry for Studying Protein Structure and Dynamics," *Chemical Society Reviews* 40 (2011): 1224.

14. L. Piersimoni, P. L. Kastritis, C. Arlt, and A. Sinz, "Cross-Linking Mass Spectrometry for Investigating Protein Conformations and Protein–Protein Interactions&bond;A Method for All Seasons," *Chemical Reviews* 122 (2022): 7500.

15. L. M. Welp, A. Wulf, A. Chernev, et al., "Chemical Crosslinking Extends and Complements UV Crosslinking in Analysis of RNA/DNA Nucleic Acid–protein Interaction Sites by Mass Spectrometry," *Nucleic Acids Research* 53 (2025): gkaf727.

16. A. Leitner, L. A. Joachimiak, P. Unverdorben, et al., "Chemical Cross-Linking/Mass Spectrometry Targeting Acidic Residues in Proteins and Protein Complexes," *Proceedings of the National Academy of Sciences of the United States of America* 111 (2014): 9455.

17. J. Chen, Q. Zhao, Y. Zhang, and L. Zhang, "In Vivo Cross-Linking Mass Spectrometry: Advances and Challenges in Decoding Protein Conformational Dynamics and Complex Regulatory Networks in Living Cells," *Current Opinion in Chemical Biology* 88 (2025): 102630.

18. A. McKenzie-Coe, N. S. Montes, and L. M. Jones, "Hydroxyl Radical Protein Footprinting: A Mass Spectrometry-Based Structural Method for Studying the Higher Order Structure of Proteins," *Chemical Reviews* 122 (2022): 7532.

19. A. K. Shaytan, H. Xiao, G. A. Armeev, et al., "Structural Interpretation of DNA–protein Hydroxyl-Radical Footprinting Experiments with High Resolution Using HYDROID," *Nature Protocols* 13 (2018): 2535.

20. J. D. Chavez, C. F. Lee, A. Caudal, A. Keller, R. Tian, and J. E. Bruce, "Chemical Crosslinking Mass Spectrometry Analysis of Protein Conformations and Supercomplexes in Heart Tissue," *Cell Systems* 6 (2018): 136.

21. J. D. Chavez, J. P. Mohr, M. Mathay, X. Zhong, A. Keller, and J. E. Bruce, "Systems Structural Biology Measurements by In Vivo Cross-Linking with Mass Spectrometry," *Nature Protocols* 14 (2019): 2318.

22. D. P. Murale, S. C. Hong, M. M. Haque, and J.-S. Lee, "Photo-Affinity Labeling (PAL) in Chemical Proteomics: A Handy Tool to Investigate Protein-Protein Interactions (PPIs)," *Proteome Science* 15 (2016): 14.

23. E. Smith and I. Collins, "Photoaffinity Labeling in Target- and Binding-Site Identification," *Future Medicinal Chemistry* 7 (2015): 159.

24. A. V. West, G. Muncipinto, H.-Y. Wu, et al., "Labeling Preferences of Diazirines with Protein Biomolecules," *Journal of the American Chemical Society* 143 (2021): 6691.

25. L. P. Conway, A. M. Jadhav, R. A. Homan, et al., "Evaluation of Fully-Functionalized Diazirine Tags for Chemical Proteomic Applications," *Chemical Science* 12 (2021): 7839.

26. K. Shiraiwa, R. Cheng, H. Nonaka, T. Tamura, and I. Hamachi, "Chemical Tools for Endogenous Protein Labeling and Profiling," *Cell Chemical Biology* 27 (2020): 970.

27. Y. Zhang, J. Tan, and Y. Chen, "Visible-Light-Induced Protein Labeling in Live Cells with Aryl Azides," *Chemical Communications* 59 (2023): 2413.

28. L. Dubinsky, B. P. Krom, and M. M. Meijler, "Diazirine Based Photoaffinity Labeling," *Bioorganic & Medicinal Chemistry* 20 (2012): 554.

29. D. Robinette, N. Neamati, K. B. Tomer, and C. H. Borchers, "Photoaffinity Labeling Combined with Mass Spectrometric Approaches as a Tool for Structural Proteomics," *Expert Review of Proteomics* 3 (2014): 399.

30. A. Walrant and E. Sachon, "Photoaffinity Labeling Coupled to MS to Identify Peptide Biological Partners: Secondary Reactions, for Better or for Worse?," *Mass Spectrometry Reviews* 44 (2025): 715.

31. K. Haupt, "Peer Reviewed: Molecularly Imprinted Polymers: The Next Generation," *Analytical Chemistry* 75 (2003): 376A.

32. J. J. BelBruno, "Molecularly Imprinted Polymers," *Chemical Reviews* 119 (2019): 94.

33. L. Chen, X. Wang, W. Lu, X. Wu, and J. Li, "Molecular Imprinting: Perspectives and Applications," *Chemical Society Reviews* 45 (2016): 2137.

34. M. Yoshikawa, K. Tharpa, and Ş.-O. Dima, "Molecularly Imprinted Membranes: Past, Present, and Future," *Chemical Reviews* 116 (2016): 11500.

35. A. Bossi, F. Bonini, A. P. F. Turner, and S. A. Piletsky, "Molecularly Imprinted Polymers for the Recognition of Proteins: The State of the Art," *Biosensors and Bioelectronics* 22 (2007): 1131.

36. S. P. B. Teixeira, R. L. Reis, N. A. Peppas, M. E. Gomes, and R. M. A. Domingues, "Epitope-Imprinted Polymers: Design Principles of Synthetic Binding Partners for Natural Biomacromolecules," *Science Advances* 7 (2021): eabi9884.

37. A. Herrera-Chacón, X. Cetó, and M. D. Valle, "Molecularly Imprinted Polymers - towards Electrochemical Sensors and Electronic Tongues," *Analytical and Bioanalytical Chemistry* 413 (2021): 6117.

38. A. M. Bossi, P. S. Sharma, L. Montana, G. Zoccatelli, O. Laub, and R. Levi, "Fingerprint-Imprinted Polymer: Rational Selection of Peptide Epitope Templates for the Determination of Proteins by Molecularly Imprinted Polymers," *Analytical Chemistry* 84 (2012): 4036.

39. S. Piletsky, F. Canfarotta, A. Poma, A. M. Bossi, and S. Piletsky, "Molecularly Imprinted Polymers for Cell Recognition," *Trends in Biotechnology* 38 (2020): 368.

40. T. Kubo, S. Arimura, Y. Tominaga, T. Naito, K. Hosoya, and K. Otsuka, "Molecularly Imprinted Polymers for Selective Adsorption of Lysozyme and Cytochrome *c* Using a PEG-Based Hydrogel: Selective Recognition for Different Conformations Due to pH Conditions," *Macromolecules* 48 (2015): 4081.

41. T. Kubo, N. Watanabe, S. Ikari, et al., "Fluorescent Detection of Target Proteins *via* a Molecularly Imprinted Hydrogel," *Analytical Methods : Advancing Methods and Applications* 13 (2021): 3086.

42. T. Kubo, H. Furuta, T. Naito, T. Sano, and K. Otsuka, "Selective Adsorption of Carbohydrates and Glycoproteins via Molecularly Imprinted Hydrogels: Application to Visible Detection by a Boronic Acid Monomer," *Chemical Communications* 53 (2017): 7290.

43. K. Kako, E. Kanao, Y. Ishihama, S. K-Yamada, and T. Kubo, "Selective Fluorescence Detection of Proteins Using Molecularly Imprinted Hydrogels with Aggregation-Induced Emission," *Journal of Materials Chemistry B* 13 (2025): 6086.

44. C. Liu, T. Kubo, and K. Otsuka, "Specific Recognition of a Target Protein, Cytochrome *c*, Using Molecularly Imprinted Hydrogels," *Journal of Materials Chemistry B* 10 (2022): 6800.

45. H. Sunayama and T. Takeuchi, "Molecularly Imprinted Protein Recognition Cavities Bearing Exchangeable Binding Sites for Postimprinting Site-Directed Introduction of Reporter Molecules for Readout of Binding Events," *ACS Applied Materials & Interfaces* 6 (2014): 20003.

46. L.-H. Liu and M. Yan, "Perfluorophenyl Azides: New Applications in Surface Functionalization and Nanomaterial Synthesis," *Accounts of Chemical Research* 43 (2010): 1434.

47. E. F. Pettersen, T. D. Goddard, C. C. Huang, et al., "UCSF Chimera—A Visualization System for Exploratory Research and Analysis," *Journal of Computational Chemistry* 25 (2004): 1605.

48. R. B. Von Dreele, "Binding of *N* -Acetylglucosamine Oligosaccharides to hen Egg-White Lysozyme: A Powder Diffraction Study," *Acta Crystallographica Section D Biological Crystallography* 61 (2005): 22.

49. S. S. Piletsky, E. Piletska, M. Poblocka, et al., "Snapshot Imprinting: Rapid Identification of Cancer Cell Surface Proteins and Epitopes Using Molecularly Imprinted Polymers," *Nano Today* 41 (2021): 101304.

50. S. A. Piletsky, T. S. Bedwell, R. Paoletti, et al., "Modulation of Acetylcholinesterase Activity Using Molecularly Imprinted Polymer Nanoparticles," *Journal of Materials Chemistry B* 10 (2022): 6732.

51. S. S. Piletsky, E. Baidyuk, E. V. Piletska, et al., "Modulation of EGFR Activity by Molecularly Imprinted Polymer Nanoparticles Targeting Intracellular Epitopes," *Nano Letters* 23 (2023): 9677.

52. E. Piletska, D. Thompson, R. Jones, et al., "Snapshot Imprinting as a Tool for Surface Mapping and Identification of Novel Biomarkers of Senescent Cells," *Nanoscale Advances* 4 (2022): 5304.

53. E. Piletska, P. Veron, B. Bertin, et al., "Analysis of Adeno-Associated Virus Serotype 8 (AAV8)-Antibody Complexes Using Epitope Mapping by Molecular Imprinting Leads to the Identification of Fab Peptides that Potentially Evade AAV8 Neutralisation," *Nanomedicine: Nanotechnology, Biology and Medicine* 52 (2023): 102691.

54. S. Mitternacht, "FreeSASA: An Open Source C Library for Solvent Accessible Surface Area Calculations," *F1000research* 5 (2016): 189.

55. M. Varadi, S. Anyango, M. Deshpande, et al., "AlphaFold Protein Structure Database: Massively Expanding the Structural Coverage of Protein-Sequence Space with High-Accuracy Models," *Nucleic Acids Research* 50 (2022): D439.

56. F. Hausch, C. Kozany, M. Theodoropoulou, and A.-K. Fabian, "FKBPs and the Akt/mTOR Pathway," *Cell Cycle* 12 (2014): 2366.

57. A. M. März, A.-K. Fabian, C. Kozany, A. Bracher, and F. Hausch, "Large FK506-Binding Proteins Shape the Pharmacology of Rapamycin," *Molecular and Cellular Biology* 33 (2013): 1357.

58. H. Nishida, E. Kanao, and Y. Ishihama, "Centrifugal Gel Crushing Tips for Gel-Based Proteome Analysis," *Analytical Chemistry* 95 (2023): 18311.

59. T. Masuda, M. Tomita, and Y. Ishihama, "Phase Transfer Surfactant-Aided Trypsin Digestion for Membrane Proteome Analysis," *Journal of Proteome Research* 7 (2008): 731.

60. J. Rappsilber, M. Mann, and Y. Ishihama, "Protocol for Micro-Purification, Enrichment, Pre-Fractionation and Storage of Peptides for Proteomics Using StageTips," *Nature Protocols* 2 (2007): 1896.

61. J. Rappsilber, Y. Ishihama, and M. Mann, "Stop and Go Extraction Tips for Matrix-Assisted Laser Desorption/Ionization, Nanoelectrospray, and LC/MS Sample Pretreatment in Proteomics," *Analytical Chemistry* 75 (2003): 663.

62. R. K. Scopes, "Measurement of Protein by Spectrophotometry at 205 nm," *Analytical Biochemistry* 59 (1974): 277.

63. Y. Ishihama, J. Rappsilber, J. S. Andersen, and M. Mann, "Microcolumns with Self-Assembled Particle Frits for Proteomics," *Journal of Chromatography A* 979 (2002): 233.

64. J. Cox and M. Mann, "MaxQuant Enables High Peptide Identification Rates, Individualized p.p.b.-Range Mass Accuracies and Proteome-Wide Protein Quantification," *Nature Biotechnology* 26 (2008): 1367.

65. J. Cox, N. Neuhauser, A. Michalski, R. A. Scheltema, J. V. Olsen, and M. Mann, "Andromeda: A Peptide Search Engine Integrated into the MaxQuant Environment," *Journal of Proteome Research* 10 (2011): 1794.

66. A. S. Hebert, S. Prasad, M. W. Belford, et al., "Comprehensive Single-Shot Proteomics with FAIMS on a Hybrid Orbitrap Mass Spectrometer," *Analytical Chemistry* 90 (2018): 9529.

67. S. Okuda, Y. Watanabe, Y. Moriya, et al., "JPOSTrepo: An International Standard Data Repository for Proteomes," *Nucleic Acids Research* 45 (2017): D1107.

Supporting Information

Additional supporting information can be found online in the Supporting Information section.